Supplementary Information for "Correlation stabilized anomalous Hall crystal in bilayer graphene"

Zhongqing Guo[1] and Jianpeng Liu[1, 2, 3, *]

[1] *School of Physical Science and Technology, ShanghaiTech University, Shanghai 201210, China*
[2] *ShanghaiTech Laboratory for Topological Physics, ShanghaiTech University, Shanghai 201210, China*
[3] *Liaoning Academy of Materials, Shenyang 110167, China*

CONTENTS

I. HARTREE-FOCK APPROXIMATION FOR TWO-DIMENSIONAL SYSTEMS

The Hartree-Fock (HF) approximation is a standard method to treat interacting electronic systems. Our HF framework is implemented in the plane-wave basis, where an electron annihilation operator $\hat{c}_\lambda(\mathbf{k})$ with flavor index λ and wavevector $\mathbf{k}$ (expanded around some low-energy valley), can be re-written as:

$$\hat{c}_{\lambda,\mathbf{G}}(\widetilde{\mathbf{k}}) \equiv \hat{c}_\lambda(\mathbf{k}), \tag{S1}$$

where $\lambda \equiv (\mu, \alpha, \sigma)$ is a composite flavor index denoting the (possible) valley, (possible) sublattice, and spin degrees of freedom. Wavevector $\mathbf{k}$ is expanded around some low-energy valley, and is further decomposed into a reciprocal vector $\mathbf{G}$ and a wavevector $\widetilde{\mathbf{k}}$ within the Brillouin zone of the corresponding lattice. The non-interacting Hamiltonian of the system can be generally expressed as:

$$H^0 = \sum_{\lambda,\lambda',\widetilde{\mathbf{k}},\mathbf{G}} H^0_{\lambda,\lambda'}(\widetilde{\mathbf{k}}+\mathbf{G})\, \hat{c}^\dagger_{\lambda,\mathbf{G}}(\widetilde{\mathbf{k}})\hat{c}_{\lambda',\mathbf{G}}(\widetilde{\mathbf{k}}). \tag{S2}$$

For the conventional two-dimensional electron gas (2DEG) system, the kinetic energy is simply given by:

$$H^0_{\mathrm{2DEG}}(\mathbf{k}) = \frac{\hbar^2\mathbf{k}^2}{2m^*}\,, \tag{S3}$$

* liujp@shanghaitech.edu.cn

where m^* is the effective mass of the electrons, $\mathbf{k} = \widetilde{\mathbf{k}} + \mathbf{G}$. For n-order Dirac fermion models, which describe n-layer graphene system, the kinetic energy term is [1, 2]:

$$H^0_{\mu,n}(\mathbf{k}) = -\begin{pmatrix} \Delta & t_\perp(\nu^\dagger_\mu)^n \\ t_\perp(\nu_\mu)^n & -\Delta \end{pmatrix}, \tag{S4}$$

where $\nu_\mu = \hbar v_F(\mu k_x + i k_y)/t_\perp$, v_F is the Fermi velocity, and $t_\perp$ is the interlayer hopping amplitude, $\mu = \mp$ denotes K/K' valley of graphene. Δ denotes the Dirac-fermion mass which physically originates from vertical electric field applied to rhombohedral multilayer graphene. Unless specified otherwise, we set $\hbar v_F = 5.25\,\mathrm{eV}\cdot\mathrm{Å}$, $t_\perp = 0.34\,\mathrm{eV}$, and $\Delta = 0.1\,\mathrm{eV}$ throughout the paper.

In this work, we consider the Coulomb interaction only in the intravalley form, neglecting the intervalley interactions, which is usually exponentially smaller than the intravalley one. This assumption simplifies the interaction Hamiltonian and is justified because intravalley interactions are generally the dominant contributions at low energies. The interaction Hamiltonian within this approximation is written as [3]:

$$H_C^{\mathrm{intra}} = \frac{1}{2N_s}\sum_{\lambda,\lambda'}\sum_{\widetilde{\mathbf{k}},\widetilde{\mathbf{k}}',\widetilde{\mathbf{q}}}\sum_{\mathbf{G},\mathbf{G}',\mathbf{Q}} V(\widetilde{\mathbf{q}}+\mathbf{Q})\hat{c}^\dagger_{\lambda,\mathbf{G}+\mathbf{Q}}(\widetilde{\mathbf{k}}+\widetilde{\mathbf{q}})\hat{c}^\dagger_{\lambda',\mathbf{G}'-\mathbf{Q}}(\widetilde{\mathbf{k}}'-\widetilde{\mathbf{q}})\hat{c}_{\lambda',\mathbf{G}'}(\widetilde{\mathbf{k}}')\hat{c}_{\lambda,\mathbf{G}}(\widetilde{\mathbf{k}}). \tag{S5}$$

Here, N_s denotes the total number of unit cells (of the presumable Wigner crystal state) in the system. Assuming that the ground state always preserves lattice translational symmetry, the expectation value of the density operator is expressed as:

$$\langle \hat{c}^\dagger_{\lambda,\mathbf{G}+\mathbf{Q}}(\widetilde{\mathbf{k}}+\widetilde{\mathbf{q}})\hat{c}_{\lambda',\mathbf{G}}(\widetilde{\mathbf{k}}')\rangle = \langle \hat{c}^\dagger_{\mu,\alpha,\mathbf{G}+\mathbf{Q}}(\widetilde{\mathbf{k}}')\hat{c}_{\mu',\alpha',\mathbf{G}}(\widetilde{\mathbf{k}}')\rangle\delta_{\widetilde{\mathbf{k}+\mathbf{q}},\widetilde{\mathbf{k}}'}\delta_{\sigma,\sigma'}. \tag{S6}$$

Then, the Hartree term reads:

$$V^{\mathrm{H}} = \frac{1}{N_s}\sum_{\widetilde{\mathbf{k}},\widetilde{\mathbf{k}}'}\sum_{\lambda,\lambda'}\sum_{\mathbf{G},\mathbf{G}',\mathbf{Q}} V(\mathbf{Q})\langle \hat{c}^\dagger_{\lambda',\mathbf{G}'-\mathbf{Q}}(\widetilde{\mathbf{k}}')\hat{c}_{\lambda',\mathbf{G}'}(\widetilde{\mathbf{k}}')\rangle\hat{c}^\dagger_{\lambda,\mathbf{G}+\mathbf{Q}}(\widetilde{\mathbf{k}})\hat{c}_{\lambda,\mathbf{G}}(\widetilde{\mathbf{k}}), \tag{S7}$$

and the Fock term reads:

$$\begin{aligned} V_{\mathrm{F}} &= -\frac{1}{N_s}\sum_{\widetilde{\mathbf{k}},\widetilde{\mathbf{k}}'}\sum_{\lambda,\lambda'}\sum_{\mathbf{G},\mathbf{G}',\mathbf{Q}} V(\widetilde{\mathbf{k}}'-\widetilde{\mathbf{k}}+\mathbf{Q})\langle \hat{c}^\dagger_{\lambda,\mathbf{G}+\mathbf{Q}}(\widetilde{\mathbf{k}}')\hat{c}_{\lambda',\mathbf{G}'}(\widetilde{\mathbf{k}}')\rangle\hat{c}^\dagger_{\lambda',\mathbf{G}'-\mathbf{Q}}(\widetilde{\mathbf{k}})\hat{c}_{\lambda,\mathbf{G}}(\widetilde{\mathbf{k}}) \\ &= -\frac{1}{N_s}\sum_{\widetilde{\mathbf{k}},\widetilde{\mathbf{k}}'}\sum_{\lambda,\lambda'}\sum_{\mathbf{G},\mathbf{G}',\mathbf{Q}} V(\widetilde{\mathbf{k}}'-\widetilde{\mathbf{k}}+\mathbf{G}'-\mathbf{G}+\mathbf{Q})\langle \hat{c}^\dagger_{\lambda,\mathbf{G}'+\mathbf{Q}}(\widetilde{\mathbf{k}}')\hat{c}_{\lambda',\mathbf{G}'}(\widetilde{\mathbf{k}}')\rangle\hat{c}^\dagger_{\lambda',\mathbf{G}-\mathbf{Q}}(\widetilde{\mathbf{k}})\hat{c}_{\lambda,\mathbf{G}}(\widetilde{\mathbf{k}}). \end{aligned} \tag{S8}$$

In these equations, $\langle \dots \rangle$ represents the expectation value of the operator in the many-body ground state $|\Psi\rangle^0$, which is assumed to be a Slater-determinant state in the HF framework. To achieve a self-consistent solution, the HF calculations are carried out iteratively for different superlattice constants L_s. The background dielectric constant is set to $\epsilon_r = 4$. To initialize the HF self-consistent loop, the expectation values of density operators $\langle \hat{c}^\dagger_{\lambda,\mathbf{G}'-\mathbf{Q}}(\widetilde{\mathbf{k}}')\hat{c}_{\lambda,\mathbf{G}'}(\widetilde{\mathbf{k}}')\rangle$ are chosen to reflect either a spontaneous charge order with non-zero Fourier component at $\mathbf{Q} \neq \mathbf{0}$, corresponding to the Wigner crystal (WC) state; or it is set to zero, corresponding to the Fermi liquid (FL) state. We compare the total energy $E_{\mathrm{total}} = E_{\mathrm{kinetic}} + E_{\mathrm{HF}}$ of these two types of states to determine the genuine ground state. Here E_{kinetic} is the kinetic energy, and E_{HF} is the HF energy including both Hartree and exchange energies. In our calculations, including HF and GW+RPA, a 9×9 mesh of reciprocal lattice points (centered at the Γ point) has been used for the 2DEG system, while a 5×5 mesh is used for n-order Dirac fermion systems. The mini Brillouin zone (of the presumable WC state) is sampled by an 18×18 $\mathbf{k}$-mesh.

II. *GW* APPROXIMATION FOR TWO-DIMENSIONAL SYSTEMS

The GW approximation provides a framework for incorporating electron-electron interactions beyond the mean-field HF theory [4–9]. It improves the description of quasiparticle (QP) energies and the single-particle energy spectrum by including the effects of dynamic screening. The key equations in the GW formalism are known as Hedin's equations, which describe a set of self-consistent equations of self-energy Σ, Green's function G, vertex function Γ, polarization propagator P, and screened Coulomb interaction W. For simplicity, here we use Arabic number as a short-hand

notation for spatial ($\mathbf{r}$) and temporal (t) coordinate, e.g., $1 \equiv (\mathbf{r}_1, t_1)$. Then, with such short-hand notations, Hedin's equations are given by:

$$\Sigma(12) = i \int \mathrm{d}3\, G(13) W(14) \Gamma(342), \tag{S9}$$

$$G(12) = G_0(12) + \int \mathrm{d}3\, G_0(13) \Sigma(34) G(42), \tag{S10}$$

$$\Gamma(123) = \delta(12)\delta(13) + \int \mathrm{d}4\, \mathrm{d}5\, \frac{\delta \Sigma(12)}{\delta G(45)} G(46) G(75) \Gamma(673), \tag{S11}$$

$$P(12) = -i \int \mathrm{d}3\, \mathrm{d}4\, G(13) G(42) \Gamma(342), \tag{S12}$$

$$W(12) = V(12) + \int \mathrm{d}3\, V(13) P(34) W(42). \tag{S13}$$

These equations form the basis of many-body perturbation theory, linking the Green's function, self-energy, and screened interaction in a self-consistent framework. To apply the GW approximation, we assume a simple form of vertex function, $\Gamma(123) = \delta(12)\delta(13)$, which leads to the "bare vertex" approximation:

$$\Gamma(123) = \delta(12)\delta(13). \tag{S14}$$

Under this approximation, the self-energy simplifies to:

$$\Sigma(12) = iG(12)W(12). \tag{S15}$$

Similarly, the polarization reduces to:

$$P(12) = -iG(12)G(21). \tag{S16}$$

To describe the screened Coulomb interaction W in terms of the dielectric function ϵ, we express V as:

$$V(12) = \int \mathrm{d}3 \epsilon(13) W(32). \tag{S17}$$

The dielectric function ϵ can be formulated as:

$$\epsilon(12) = \delta(12) - \int \mathrm{d}3 V(13) P(32). \tag{S18}$$

We continue to perform a Fourier transform from time domain to frequency domain to handle the time-dependent components. Now we go back to the usual notations where $\mathbf{r}$ ($\mathbf{r}'$) denote real-space coordinate, and ω denote frequency. The non-interacting Green's function G_0 is given by:

$$G_0(\mathbf{r}, \mathbf{r}', \omega) = \sum_{n\widetilde{\mathbf{k}}} \frac{\psi_{n\widetilde{\mathbf{k}}}(\mathbf{r}) \psi^*_{n\widetilde{\mathbf{k}}}(\mathbf{r}')}{\omega - \varepsilon_{n\widetilde{\mathbf{k}}} + i\delta \mathrm{sgn}(\varepsilon_{n\widetilde{\mathbf{k}}} - \varepsilon_F)}, \tag{S19}$$

where $\psi_{n\widetilde{\mathbf{k}}}$ are the HF single-particle wave functions, $\varepsilon_{n\widetilde{\mathbf{k}}}$ are the HF eigenvalues, and ε_F is the Fermi energy. The non-interacting charge polarizability χ^0, which characterizes the linear response of the system to external perturbative potentials, is given by:

$$\chi^0(\mathbf{r}, \mathbf{r}', \nu) = -i \int \frac{\mathrm{d}\omega}{2\pi} e^{i\omega\delta^+} G_0(\mathbf{r}, \mathbf{r}', \omega + \nu) G_0(\mathbf{r}', \mathbf{r}, \omega). \tag{S20}$$

Using χ^0, the dielectric function within the Random Phase Approximation (RPA) is expressed as:

$$\epsilon_{\mathrm{RPA}}(\mathbf{r}, \mathbf{r}', \omega) = \delta(\mathbf{r}, \mathbf{r}') - \int \mathrm{d}\mathbf{r}'' V(\mathbf{r}, \mathbf{r}'') \chi^0(\mathbf{r}'', \mathbf{r}', \omega). \tag{S21}$$

The screened Coulomb interaction within RPA is:

$$W_{\mathrm{RPA}}(\mathbf{r},\mathbf{r}',\omega)=\int \mathrm{d}\mathbf{r}''\left[\epsilon^{-1}_{\mathrm{RPA}}(\mathbf{r},\mathbf{r}'',\omega)-\delta(\mathbf{r},\mathbf{r}'')\right]V(\mathbf{r}'',\mathbf{r}'), \tag{S22}$$

where the static part has been subtracted as it is already taken into account in the HF calculations. The correlation part of the self-energy, Σ_c, which accounts for electron correlation effects beyond HF, is then computed using:

$$\Sigma_c(\mathbf{r},\mathbf{r}',\omega)=\frac{i}{2\pi}\int d\nu\, e^{i\nu\delta^+}G_0(\mathbf{r},\mathbf{r}',\omega+\nu)W_{\mathrm{RPA}}(\mathbf{r}',\mathbf{r},\nu), \tag{S23}$$

where G_0 is the HF Green's function and W_{RPA} is the dynamically screened Coulomb interaction.

Then, we perform a Fourier transform from real space to reciprocal space. The matrix elements of the non-interacting charge polarizability in reciprocal space are:

$$\begin{aligned}\chi^0_{\mathbf{QQ}'}(\widetilde{\mathbf{q}},\nu)=&\frac{1}{N\Omega_0}\sum_{n',n,\widetilde{\mathbf{k}}}\left[\sum_{\lambda,\mathbf{G}}C^*_{\lambda\mathbf{G}+\mathbf{Q},n'\widetilde{\mathbf{k}}+\widetilde{\mathbf{q}}}C_{\lambda\mathbf{G},n\widetilde{\mathbf{k}}}\right]^*\left[\sum_{\lambda',\mathbf{G}'}C^*_{\lambda'\mathbf{G}'+\mathbf{Q}',n'\widetilde{\mathbf{k}}+\widetilde{\mathbf{q}}}C_{\lambda'\mathbf{G}',n\widetilde{\mathbf{k}}}\right]\\&\times\left[\frac{\theta(\varepsilon_{n'\widetilde{\mathbf{k}}+\widetilde{\mathbf{q}}}-\varepsilon_F)\theta(\varepsilon_F-\varepsilon_{n\widetilde{\mathbf{k}}})}{\nu-\varepsilon_{n'\widetilde{\mathbf{k}}+\widetilde{\mathbf{q}}}+\varepsilon_{n\widetilde{\mathbf{k}}}+i\delta}-\frac{\theta(\varepsilon_F-\varepsilon_{n'\widetilde{\mathbf{k}}+\widetilde{\mathbf{q}}})\theta(\varepsilon_{n\widetilde{\mathbf{k}}}-\varepsilon_F)}{\nu-\varepsilon_{n'\widetilde{\mathbf{k}}+\widetilde{\mathbf{q}}}+\varepsilon_{n\widetilde{\mathbf{k}}}-i\delta}\right],\end{aligned}$$

where $C_{\lambda\mathbf{G},n\widetilde{\mathbf{k}}}$ are the expansion coefficients of the single-particle states in the plane-wave basis, and $\mathbf{G}$, $\mathbf{G}'$, $\mathbf{Q}$, and $\mathbf{Q}'$ denote reciprocal vectors. The matrix form of the RPA dielectric function in reciprocal space is expressed as:

$$\epsilon^{\mathrm{RPA}}_{\mathbf{QQ}'}(\widetilde{\mathbf{q}},\omega)=\delta_{\mathbf{QQ}'}-V(\widetilde{\mathbf{q}}+\mathbf{Q})\chi^0_{\mathbf{QQ}'}(\widetilde{\mathbf{q}},\omega), \tag{S24}$$

and the screened Coulomb interaction in reciprocal space is given by:

$$W^{\mathrm{RPA}}_{\mathbf{QQ}'}(\widetilde{\mathbf{q}},\omega)=\left[\epsilon^{-1,\mathrm{RPA}}_{\mathbf{QQ}'}(\widetilde{\mathbf{q}},\omega)-\delta_{\mathbf{QQ}'}\right]V(\widetilde{\mathbf{q}}+\mathbf{Q}'). \tag{S25}$$

The correlation self-energy in reciprocal space can be expressed as:

$$\begin{aligned}\Sigma_c(\widetilde{\mathbf{k}},\omega)_{nn}=&\frac{i}{N\Omega_0}\sum_{m,\widetilde{\mathbf{q}}}\sum_{\mathbf{G},\mathbf{G}'}\left[\sum_{\lambda,\mathbf{Q}}C^*_{\lambda\mathbf{G}+\mathbf{Q},m\widetilde{\mathbf{k}}+\widetilde{\mathbf{q}}}C_{\lambda\mathbf{Q},n\widetilde{\mathbf{k}}}\right]^*\left[\sum_{\lambda',\mathbf{Q}'}C^*_{\lambda'\mathbf{G}'+\mathbf{Q}',m\widetilde{\mathbf{k}}+\widetilde{\mathbf{q}}}C_{\lambda'\mathbf{Q}',n\widetilde{\mathbf{k}}}\right]\\&\times V(\widetilde{\mathbf{q}}+\mathbf{G})\int\frac{\mathrm{d}\nu}{2\pi}e^{i\nu\eta}\frac{\left[\epsilon^{-1,\mathrm{RPA}}_{\mathbf{G}'\mathbf{G}}(\widetilde{\mathbf{q}},\nu)-\delta_{\mathbf{GG}'}\right]}{\omega+\nu-\varepsilon_{m\widetilde{\mathbf{k}}+\widetilde{\mathbf{q}}}+i\delta\mathrm{sgn}(\varepsilon_{m\widetilde{\mathbf{k}}+\widetilde{\mathbf{q}}}-\varepsilon_F)}.\end{aligned}$$

In this formalism, the inverse dielectric function $\epsilon^{-1}_{\mathrm{RPA}}$ plays a critical role in capturing the frequency-dependent screening of the Coulomb interaction. The QP energies are then corrected through the GW self-energy, expressed as:

$$\varepsilon^{\mathrm{QP}}_{n\widetilde{\mathbf{k}}}=\varepsilon^{\mathrm{HF}}_{n\widetilde{\mathbf{k}}}+Z_{n\widetilde{\mathbf{k}}}\,\mathrm{Re}\,\Sigma_c(\widetilde{\mathbf{k}},\varepsilon^{\mathrm{HF}}_{n\widetilde{\mathbf{k}}})_{nn}, \tag{S26}$$

where $Z_{n\widetilde{\mathbf{k}}}$ is the QP weight, accounting for interaction renormalization effects of QPs:

$$Z_{n\widetilde{\mathbf{k}}}=\left[1-\mathrm{Re}\left(\frac{\partial\Sigma_c(\widetilde{\mathbf{k}},\omega)_{nn}}{\partial\omega}\right)_{\omega=\varepsilon^{\mathrm{HF}}_{n\widetilde{\mathbf{k}}}}\right]^{-1}. \tag{S27}$$

This procedure enables a more accurate determination of the single-particle energy spectrum and the QP energies by including the effects of electron correlation and dynamic screening, improving upon the HF approximation.

In Supplementary Figure. 1(a), we present the energy spectrum of Dirac fermions in monolayer graphene after HF calculations with 10% electron doping with respect to charge neutrality, incorporating the GW self-energy correction. The main HF bands are clearly visible, along with surrounding satellite features. These satellites arise from electron-plasmon interactions, representing plasmaron or plasmon-polaron states, consistent with previous theoretical and experimental reports [10–12]. In Supplementary Figure. 1(b), we show the collective excitation spectrum corresponding to Supplementary Figure. 1(a). In the limit where q approaches 0, it display the typical $\sqrt{q}$ dependence, indicating the presence of a gapless plasmon mode, which implies the prominent satellite feature in the GW single-particle excitation spectra.

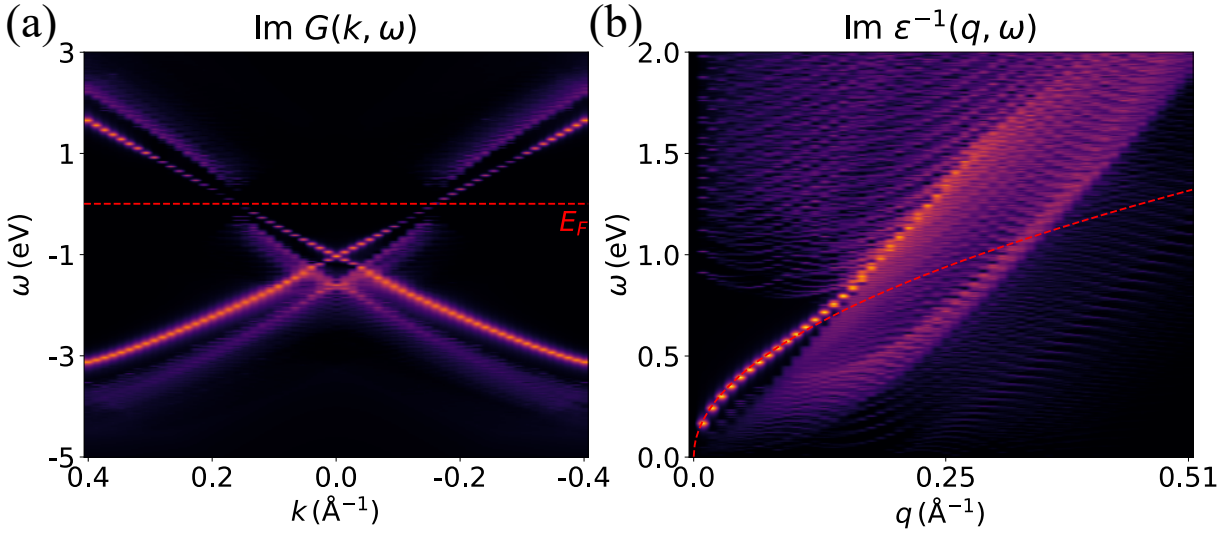

Supplementary Figure 1: (a) Energy spectrum of Dirac fermions in monolayer graphene with 10% electron doping. (b) Collective excitation spectrum.

III. MULTIPLE PLASMON POLE APPROXIMATION (MPA)

The multiple plasmon pole approximation (MPA) [13, 14] is an improvement over the single plasmon pole model (PPA) [5, 15–18] used to approximate the dielectric function. Instead of approximating the dielectric function using a single plasmon mode, the MPA assumes the existence of multiple particle-hole collective excitations (they are all called "plasma" for simplicity). The dielectric function is then fitted using these multiple plasma (collective-excitation) modes. The approximation is given by:

$$\epsilon^{-1,MPA}_{\mathbf{QQ}'}(\widetilde{\mathbf{q}},\nu)-\delta_{\mathbf{QQ}'}=\sum_{l}^{N_p}\frac{2R_{l,\mathbf{QQ}'}(\widetilde{\mathbf{q}})\Omega_{l,\mathbf{QQ}'}(\widetilde{\mathbf{q}})}{\nu^2-\Omega^2_{l,\mathbf{QQ}'}(\widetilde{\mathbf{q}})}, \tag{S28}$$

where N_p represents the number of plasmon poles, while R and Ω are parameters to be determined. Specifically, $R_{l,\mathbf{QQ}'}(\widetilde{\mathbf{q}})$ denotes the residue of the l-th plasmon mode, and $\Omega_{l,\mathbf{QQ}'}(\widetilde{\mathbf{q}})$ represents its frequency. To solve for these unknown parameters, we require the values of the dielectric function at $2N_p$ different frequencies.

The advantage of the MPA is that it can simultaneously describe both plasmon modes and the continuous spectrum, avoiding the need for complicated frequency integrations, which greatly speeds up the calculation. Moreover, the accuracy of the approximation can be controlled by adjusting the number of poles in the model, allowing for a balance between computational efficiency and precision. This is especially useful for the spontaneous-symmetry breaking states such as Wigner crystal, where there are multiple collective modes such as acoustic and optical quantum phonons [19].

Supplementary Figure 2 shows some typical examples of the comparison between the numerically calculated inverse dielectric function (dashed lines) and the MPA-fitted inverse dielectric function (solid lines). The red and blue lines correspond to the real and imaginary parts of the inverse dielectric function, respectively. Supplementary Figure 2(a) presents the case of small $\widetilde{\mathbf{q}}$ with $\mathbf{G}=0$ near the Γ point, where a clear plasmon mode is visible near $q=0$. The MPA approximation accurately captures this plasmon mode and also describes the continuum part of the dielectric function at higher frequencies. In Supplementary Figure 2(b), where $\mathbf{G}\neq 0$ and away from the Γ point, the system enters the continuum spectrum region of the inverse dielectric function. The MPA approximation successfully describes the continuous spectrum using multiple plasmons, a task beyond the capability of the single plasmon pole model. Additionally, the oscillations in the numerically computed inverse dielectric function caused by $\mathbf{k}$-mesh discretization (or finite-size effects) are smoothed out using MPA. Supplementary Figures 2(c) and 2(d) show the off-diagonal elements of the inverse dielectric function, both near and far from the Γ point. Although these elements are relatively small, the MPA still provides an accurate description.

Using the MPA, we can compute the correlation self-energy more efficiently without losing accuracy. The correlation

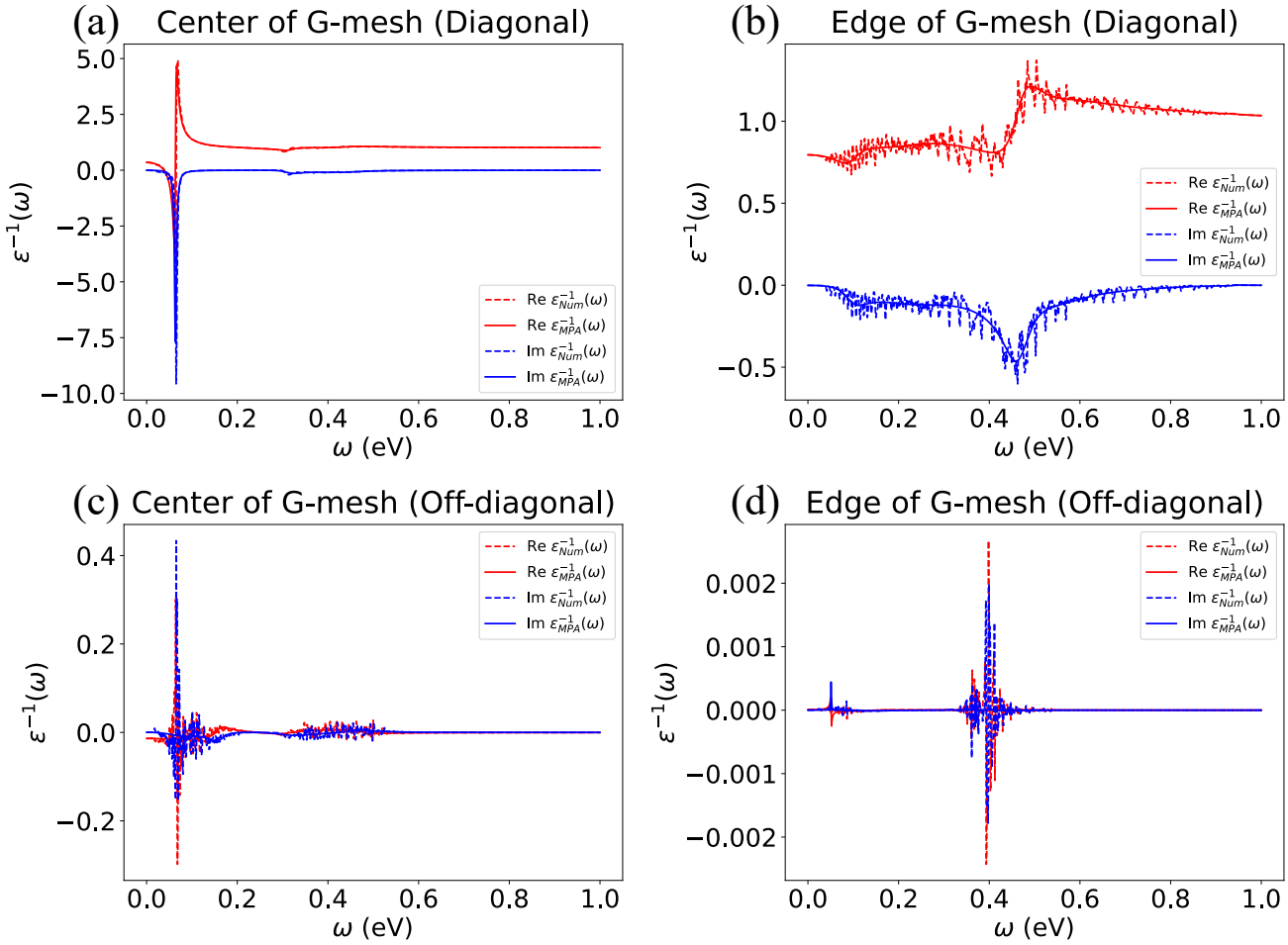

Supplementary Figure 2: Comparison between the numerically calculated inverse dielectric function (dashed lines) and the MPA-fitted inverse dielectric function (solid lines). The real part is shown in red, and the imaginary part is shown in blue. (a) Small $\tilde{\mathbf{q}}$ with $\mathbf{G} = 0$ near the Γ point, showing a prominent plasmon mode near $q = 0$. (b) Non-zero $\mathbf{G}$ away from the Γ point, entering the continuum spectrum region. (c) and (d) Off-diagonal elements near and away from the Γ point.

self-energy Σ_c in the MPA is given by:

$$\Sigma_c(\tilde{\mathbf{k}},\omega)_{nn} = \frac{1}{N\Omega_0}\sum_{m,\tilde{\mathbf{q}}}\sum_{\mathbf{G},\mathbf{G}'}\left[\sum_{\lambda,\mathbf{Q}} C^*_{\lambda\mathbf{G}+\mathbf{Q},m\tilde{\mathbf{k}}+\tilde{\mathbf{q}}} C_{\lambda\mathbf{Q},n\tilde{\mathbf{k}}}\right]^* \left[\sum_{\lambda',\mathbf{Q}'} C^*_{\lambda'\mathbf{G}'+\mathbf{Q}',m\tilde{\mathbf{k}}+\tilde{\mathbf{q}}} C_{\lambda'\mathbf{Q}',n\tilde{\mathbf{k}}}\right] \times \sum_{l}^{N_p} \frac{V(\tilde{\mathbf{q}}+\mathbf{G}) R_{\mathbf{G}'\mathbf{G},l}(\tilde{\mathbf{q}})}{\omega - \varepsilon_{m\tilde{\mathbf{k}}+\tilde{\mathbf{q}}} + i\delta\mathrm{sgn}(\varepsilon_{m\tilde{\mathbf{k}}+\tilde{\mathbf{q}}} - \varepsilon_F) + \Omega_{\mathbf{G}'\mathbf{G},l}(\tilde{\mathbf{q}})(2f_{m\tilde{\mathbf{k}}+\tilde{\mathbf{q}}} - 1)}, \tag{S29}$$

where $f_{m\tilde{\mathbf{k}}+\tilde{\mathbf{q}}}$ represents the Fermi-Dirac distribution function. The derivative of the correlation self-energy with respect to ω is required to determine the QP weight $Z_{n\tilde{\mathbf{k}}}$:

$$\frac{\partial\Sigma_c(\tilde{\mathbf{k}},\omega)_{nn}}{\partial\omega} = \frac{-1}{N\Omega_0}\sum_{m,\tilde{\mathbf{q}}}\sum_{\mathbf{G},\mathbf{G}'}\left[\sum_{\lambda,\mathbf{Q}} C^*_{\lambda\mathbf{G}+\mathbf{Q},m\tilde{\mathbf{k}}+\tilde{\mathbf{q}}} C_{\lambda\mathbf{Q},n\tilde{\mathbf{k}}}\right]^* \left[\sum_{\lambda',\mathbf{Q}'} C^*_{\lambda'\mathbf{G}'+\mathbf{Q}',m\tilde{\mathbf{k}}+\tilde{\mathbf{q}}} C_{\lambda'\mathbf{Q}',n\tilde{\mathbf{k}}}\right] \times \sum_{l}^{N_p} \frac{V(\tilde{\mathbf{q}}+\mathbf{G}) R_{\mathbf{G}'\mathbf{G},l}(\tilde{\mathbf{q}})}{\left[\omega - \varepsilon_{m\tilde{\mathbf{k}}+\tilde{\mathbf{q}}} + i\delta\mathrm{sgn}(\varepsilon_{m\tilde{\mathbf{k}}+\tilde{\mathbf{q}}} - \varepsilon_F) + \Omega_{\mathbf{G}'\mathbf{G},l}(\tilde{\mathbf{q}})(2f_{m\tilde{\mathbf{k}}+\tilde{\mathbf{q}}} - 1)\right]^2}. \tag{S30}$$

In the MPA, by fitting the dielectric function using multiple plasma modes, we can more accurately capture the collective excitations of the system, including both collective modes described by poles and the continuum spectra. This approach not only enhances the precision of the calculations but also significantly improves computational efficiency by reducing the complexity of frequency integration.

IV. RANDOM PHASE APPROXIMATION FOR CORRELATION ENERGY

The total energy of the system within RPA framework is given by:

$$E_{\text{tot.}} = E_{\text{kin.}} + E_{\text{HF}} + E_c^{\text{RPA}}, \tag{S31}$$

where $E_{\text{kin.}}$ is the kinetic energy, E_{HF} is the HF energy, and E_c^{RPA} represents the correlation energy obtained through the RPA. The inclusion of E_c^{RPA} is crucial, as the HF approximation alone neglects correlation effects, leading to an overestimation of the tendency for symmetry-breaking states such as WC. The RPA provides a more accurate description by incorporating the effects of electron-electron interactions beyond the mean-field level.

The correlation energy in the RPA is given by [20–23]:

$$\begin{aligned} E_c^{\text{RPA}} &= \frac{1}{4\pi}\int_{-\infty}^{\infty} \mathrm{d}\omega\, \mathrm{Tr}\left\{\ln\left[1 - V\chi^0(i\omega)\right] + V\chi^0(i\omega)\right\} \\ &= \frac{1}{4\pi}\int_{-\infty}^{\infty} \mathrm{d}\omega \sum_{\widetilde{\mathbf{q}},\mathbf{Q},\mathbf{Q}'} \left\{\ln\left[\delta_{\mathbf{Q}\mathbf{Q}'} - V_{\mathbf{Q}}\delta_{\mathbf{Q}\mathbf{Q}'}\chi^0_{\mathbf{Q}'\mathbf{Q}}(\widetilde{\mathbf{q}}, i\omega)\right] + V_{\mathbf{Q}}\delta_{\mathbf{Q}\mathbf{Q}'}\chi^0_{\mathbf{Q}'\mathbf{Q}}(\widetilde{\mathbf{q}}, i\omega)\right\}, \end{aligned}$$

where V is the bare Coulomb interaction, and $\chi^0(i\omega)$ calculated by S24 is the non-interacting charge polarizability in the imaginary frequency domain. The first line of the equation presents a general expression for the RPA correlation energy in matrix form, involving a trace over all possible interaction channels. The second line expands this expression into the momentum space, where $\widetilde{\mathbf{q}}$ and $\mathbf{Q}$ denote momentum vectors, and $\chi^0_{\mathbf{Q}'\mathbf{Q}}(\widetilde{\mathbf{q}}, i\omega)$ are the matrix elements of the non-interacting susceptibility.

By combining the *GW* approximation and the RPA, we achieve a more comprehensive description of the total energy. The *GW* approximation improves the single-particle energy spectrum, leading to more accurate values for $\chi^0(i\omega)$, while the RPA incorporates the dynamic charge fluctuation effects to provide a more reliable estimate of the correlation energy. This approach is essential for capturing the delicate balance between the FL state and other competing spontaneous symmetry-breaking phases, such as the WC state, especially in low-carrier-density interacting two-dimensional systems.

V. DATA FITTING FOR CRITICAL WIGNER-SEITZ RADIUS r_s^* IN 2DEG

To determine the critical Wigner-Seitz radius r_s^* for the transition between the FL state and the WC state in 2DEG system, we perform a detailed data fitting analysis. The total energies of both the WC and FL states are calculated using the *GW*+RPA framework, which incorporates both the exchange and correlation effects more accurately compared to the HF approximation.

The energy of the Wigner crystal state E_{WC} is fitted using the following expression [24]:

$$E_{\text{WC}} = \frac{c_1}{r_s} + \frac{c_{3/2}}{r_s^{3/2}} + \frac{c_2}{r_s^2} + \frac{c_{5/2}}{r_s^{5/2}} + \frac{c_3}{r_s^3}, \tag{S32}$$

where the coefficients c_1, $c_{3/2}$, c_2, $c_{5/2}$, and c_3 are fitting parameters that capture the behavior of the WC state as a function of the Wigner-Seitz radius r_s. These terms account for various contributions to the energy, including kinetic, exchange, and correlation energies. The form of this equation ensures a smooth interpolation of the energy in the WC state regime.

For the Fermi liquid state, the total energy E_{FL} is composed of two parts: the Hartree-Fock energy $E_{\text{FL}}^{\text{HF}}$ and the correlation energy E_{FL}^c [25]:

$$E_{\text{FL}} = E_{\text{FL}}^{\text{HF}} + E_{\text{FL}}^c. \tag{S33}$$

The Hartree-Fock energy for the FL state is given by:

$$E_{\text{FL}}^{\text{HF}} = \frac{1}{2r_s^2} - \frac{4\sqrt{2}}{3\pi r_s}, \tag{S34}$$

where the first term represents the kinetic energy contribution, and the second term accounts for the exchange energy in the FL state. However, the Hartree-Fock approximation alone does not include correlation effects, which are crucial for accurately capturing the properties of the FL state.

To include the correlation effects, we use an empirical formula for the correlation energy E_{FL}^{c}:

$$E_{\mathrm{FL}}^{c}=a_0\left\{1+Ax^2\left[B\ln\frac{x+a_1}{x}+C\ln\frac{\sqrt{x^2+2a_2x+a_3}}{x}+D\left(\arctan\frac{x+a_2}{\sqrt{a_3-a_2^2}}-\frac{\pi}{2}\right)\right]\right\}, \tag{S35}$$

where $x=\sqrt{r_s}$. The parameters a_0, a_1, a_2, and a_3 are fitting parameters that are determined through numerical fitting to the GW+RPA data. The coefficients A, B, C, and D are given by:

$$A=\frac{2(a_1+2a_2)}{2a_1a_2-a_3-a_1^2}, \tag{S36}$$

$$B=\frac{1}{a_1}-\frac{1}{a_1+2a_2}, \tag{S37}$$

$$C=\frac{a_1-2a_2}{a_3}+\frac{1}{a_1+2a_2}, \tag{S38}$$

$$D=\frac{F-a_2C}{\sqrt{a_3-a_2^2}}, \tag{S39}$$

$$F=1+(2a_2-a_1)\left(\frac{1}{a_1+2a_2}-\frac{2a_2}{a_3}\right). \tag{S40}$$

These expressions are derived to provide an accurate representation of the correlation energy in the FL state, taking into account the complex interaction effects in the 2DEG. The GW+RPA method gives a more precise calculation of χ^0, leading to a reliable estimation of the correlation energy.

By fitting the total energies E_{WC} and E_{FL} obtained from the GW+RPA calculations, we identify the critical Wigner-Seitz radius r_s^* where the energies of the WC and FL states intersect. This intersection marks the transition point between the gapless Fermi liquid state and the charge-gapped Wigner crystal state. In our calculations for the conventional 2DEG system, this critical value is found to be $r_s^*\sim 19.2$, significantly improving upon the values obtained from the HF or HF+RPA calculations. This refined critical radius demonstrates the importance of accurately including correlation effects through the GW+RPA framework when studying phase transitions in interacting electron systems.

VI. MORE RESULTS ABOUT n-ORDER DIRAC FERMION MODELS FOR n=2, 3, 4, 5, AND 6

A. HF results

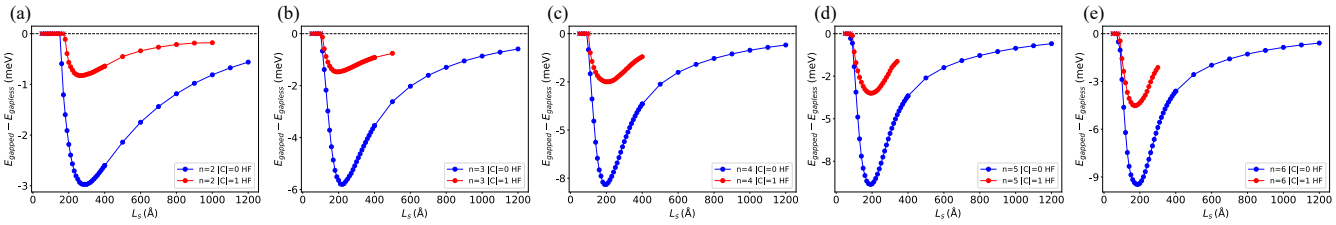

Supplementary Figure 3: (a)-(e) The HF results for the WC condensation energy as a function of lattice constant L_s for n-order Dirac fermion models with $n=2$ to 6, respectively.

Supplementary Figure 3 shows the HF results for the WC condensation energy as a function of lattice constant L_s for n-order Dirac fermion models with $n=2$ to 6. For $n=2$ to 6 layers (corresponding to Supplementary

Figures 3(a)-(e)), the HF ground states for all cases are the trivial WC states. Additionally, there exists a metastable anomalous Hall crystal (AHC) state at certain values of L_s for each case. However, the Chern-number-1 ground states cannot stably exist at lower electron densities, as indicated by the cutoffs at the right end of the red lines in the figures, where the Chern-number-1 metastable states under HF self-consistent calculation converge to Chern-number-0 ground states. As the number of layers increases, the condensation energies of both types of WC states at the same L_s would increase in amplitude, indicating that the WC states become more stable with higher layer numbers within HF framework. This is due to the fact that systems with more layers exhibit higher density of states near Fermi energy, which further enhances interaction effects and stabilizes the WC states.

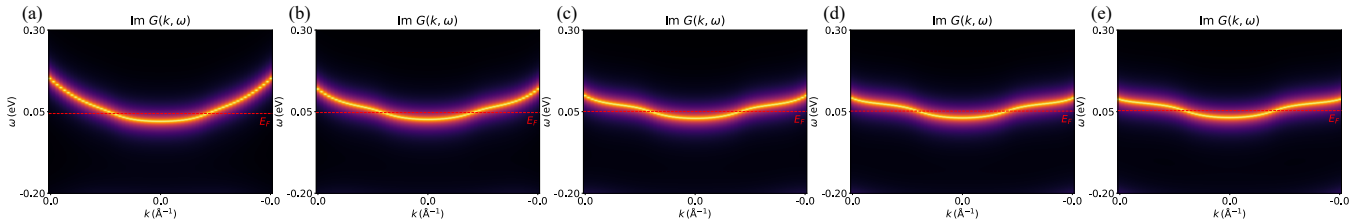

Supplementary Figure 4: (a)-(e) The HF single-particle energy spectra of the FL state for n-order Dirac fermion models with $n = 2$ to 6 at $L_s = 200$ Å, respectively. The red dashed lines mark the Fermi energies.

Supplementary Figures 4(a)-(e) show the HF single-particle energy spectra of the FL state at for n-order Dirac fermion models with $n = 2$ to 6 at $L_s = 200$ Å, respectively. As the number of layers increases from $n = 2$ to $n = 6$, the low-energy bands become increasingly less dispersive, indicating stronger correlation effects with higher n. For lower n, such as in Supplementary Figure 4(a) and (b), the bands near the Fermi surface retain a relatively more dispersive character. However, as seen in Supplementary Figure 4(c)-(e), the bands flatten further, showing the enhanced influence of electron-electron interactions as the layer number increases.

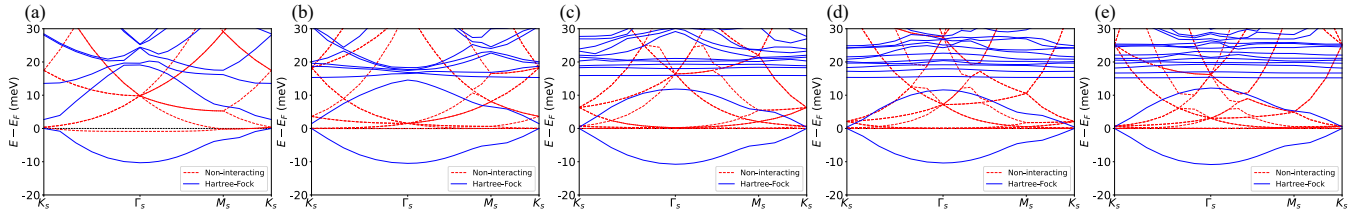

Supplementary Figure 5: (a)-(e) The HF band structures for the AHC state for n-order Dirac fermion models with $n = 2$ to 6 at $L_s = 200$ Å, respectively. The gray dashed lines mark the Fermi energies.

Supplementary Figures 5(a)-(e) present the HF band structures for the AHC state for n-order Dirac fermion models with $n = 2$ to 6 at $L_s = 200$ Å, respectively. The red dashed lines indicate the non-interacting results, where it can be observed that as n increases, the low-energy bands become significantly flatter. The blue solid lines show the HF results, where an increase in n leads to a gradual reduction in the bandwidth before $n = 4$, and the band structures barely vary after $n = 4$.

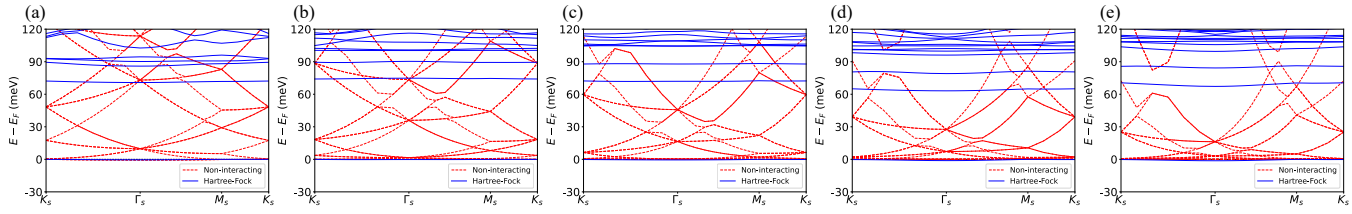

Supplementary Figure 6: (a)-(e) The HF band structures for the trivial WC state for n-order Dirac fermion models with $n = 2$ to 6 at $L_s = 200$ Å, respectively.

Supplementary Figures 6(a)-(e) display the HF band structures for the trivial WC state for n-order Dirac fermion models with $n = 2$ to 6 at $L_s = 200$ Å, respectively, in comparison with the Chern-number-1 bands shown in Supplementary Figure 5. As n increases, a key difference emerges: the low-energy bands in the Chern-number-0 state are more flat compared to those in the Chern-number-1 state, indicating a relatively stronger interaction-induced

renormalization. In contrast to the Chern-number-1 state, the bandwidth of the Chern-number-0 state does not increase significantly due to interactions. This indicates a stronger tendency for electron localization in the Chern-number-0 state. This observation is consistent with the real-space charge distribution discussed in the main text, where electrons in the Chern-number-0 state form a more localized charge pattern.

B. GW+RPA Results

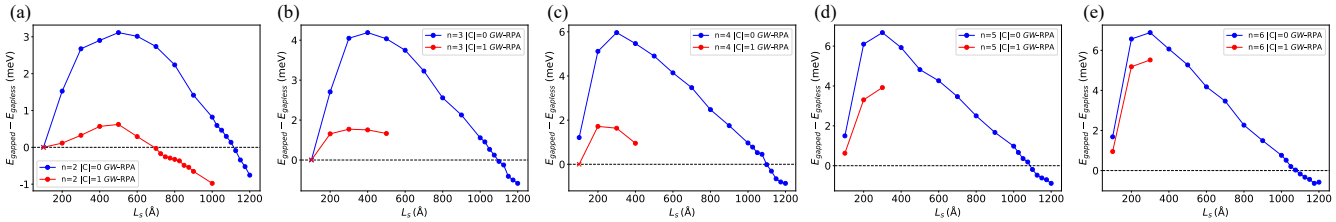

Supplementary Figure 7: (a)-(e) The GW+RPA results for the WC condensation energy as a function of lattice constant L_s for n-order Dirac fermion models with $n = 2$ to 6, respectively.

Compared to the HF ground-state results in Supplementary Figure 3, the GW+RPA approach yields significantly different results. For the trivial WC state, similar to the 2DEG case, the more accurate GW+RPA method further enhances the effect of RPA correlation energy, which mitigates the overestimated exchange energy that stabilizes the WC state. This adjustment causes the phase transition for the trivial WC to occur at lower electron densities, with the layer separation increasing from approximately $L_s \sim 100\,\text{Å}$ to $\sim 1100\,\text{Å}$ across various layers. For the AHC, the average energy gap above and below the Fermi surface is significantly smaller than in the trivial WC, leading to a substantially larger RPA correlation energy. As shown in the results from the GW+RPA calculations, the total energy of the AHC remains consistently lower than that of the trivial WC. Specifically, in the case of $n = 2$, our calculations indicate a AHC ground state for L_s values above 700 Å (corresponding to a critical density $\sim 2.4 \times 10^{10}\text{cm}^{-2}$). These findings illustrate that the correlation energy provided by the GW+RPA approach is crucial in Dirac-fermion systems, effectively mitigating the exchange energy's overestimation of WC stability and yielding a more accurate depiction of the ground state.

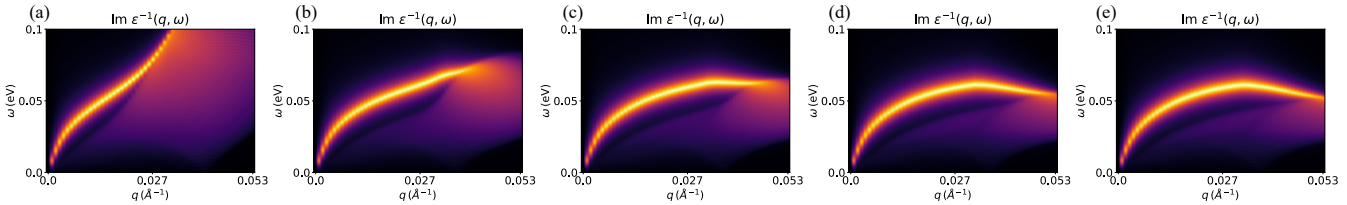

Supplementary Figure 8: (a)-(e) The electron excitation spectra calculated based on the HF band for the trivial WC state for n-order Dirac fermion models with $n = 2$ to 6 at $L_s = 200\,\text{Å}$, respectively.

Supplementary Figures 8(a)-(e) show the collective excitation spectra for n-order Dirac fermion models with $n = 2$ to 6 at $L_s = 200\,\text{Å}$, respectively, calculated based on the HF energy bands. Here we focus on the most significant intraband low-energy collective excitations. Besides the particle-hole continuum, in the limit where q approaches 0, all layers display the typical $\sqrt{q}$ dependence, indicating the presence of a gapless plasmon mode. However, the bandwidth of these modes differs notably in the $n = 2, 3, 4$ systems. As the layer number increases to $n = 5$ and $n = 6$, the HF bands become extremely flat, and the collective excitation spectra exhibit a weakly dispersive branch over a certain range of wavevector. This behavior implies the presence of a prominent satellite feature in the GW single-particle excitation spectra.

Supplementary Figures 9(a)-(e) show the GW-calculated single-particle energy spectra for the FL state for n-order Dirac fermion models with $n = 2$ to 6 at $L_s = 200\,\text{Å}$, respectively. Near the Fermi surface, distinct plasmon satellites are visible, indicating the influence of electron-plasmon interactions. Furthermore, as shown in Supplementary Figure 8, with increasing layer number, a progressively flatter and nearly momentum-independent spectral feature emerges below the Fermi surface. This flat feature arises from the interaction between electrons and plasmons, leading to the formation of plasmarons or plasma-polarons. Similar features in the single-particle spectra due to electron-plasmon couplings have also been reported in carrier-doped monolayer graphene [10–12]. The appearance of this

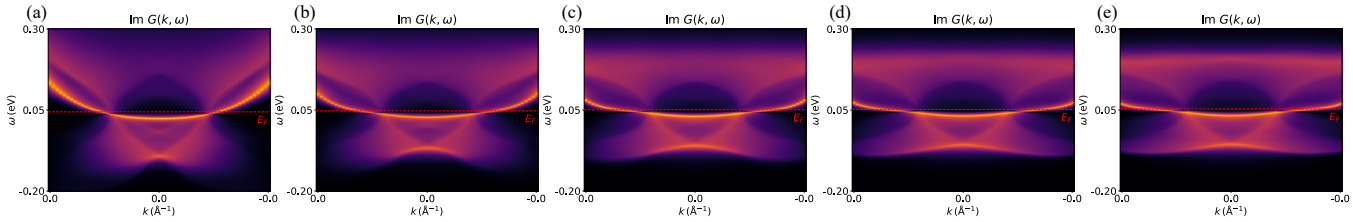

Supplementary Figure 9: (a)-(e) The GW-calculated single-particle energy spectra for the FL state for n-order Dirac fermion models with $n = 2$ to 6 at $L_s = 200$ Å, respectively.

feature becomes more pronounced with smaller bandwidth in higher-layer systems, resulting from the flatter bands in the corresponding non-interacting models.

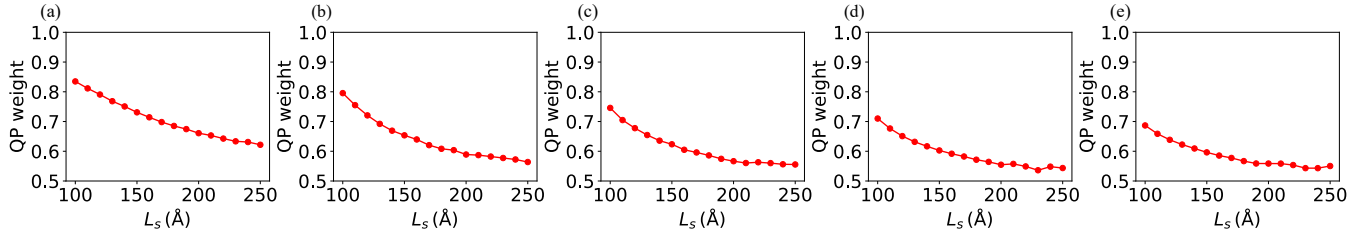

Supplementary Figure 10: (a)-(e) The GW-calculated QP weight for the FL state for n-order Dirac fermion models with $n = 2$ to 6, respectively.

Supplementary Figures 10(a)-(e) show the GW-calculated QP weight for the FL state for n-order Dirac fermion models with $n = 2$ to 6, respectively. As the layer number n increases, the QP weight at the same L_s gradually decreases, indicating a reduction in the coherent part of the spectral weight. This reduction reflects the increasing interaction effects in higher-layer systems, consistent with the enhanced electron-plasmon interactions observed in the corresponding GW single-particle spectra.

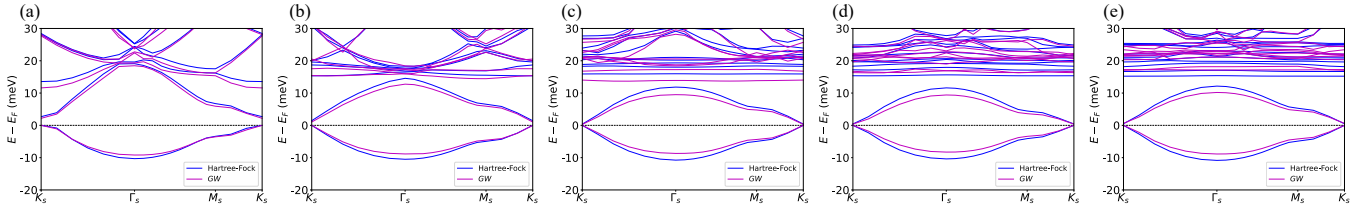

Supplementary Figure 11: (a)-(e) The GW-calculated single-particle energy spectra for the AHC state for n-order Dirac fermion models with $n = 2$ to 6 at $L_s = 200$ Å, respectively.

Supplementary Figures 11(a)-(e) and Supplementary Figures 12(a)-(e) show the GW quasi-particle band structures for the AHC and trivial WC states for n-order Dirac fermion models with $n = 2$ to 6 at $L_s = 200$ Å, respectively, compared to the HF results in Supplementary Figures 5(a)-(e) and Supplementary Figures 6(a)-(e). The GW correction introduces dynamical screening of the Coulomb interactions, resulting in a more accurate calculation of the bandwidth and band gap. This correction mitigates the overestimation by the HF approximation, leading to a reduced bandwidth and a more realistic depiction of the gap.

C. Trigonal warping effects in bilayer graphene (BLG)

We continue to present results about the more realistic bilayer graphene two-band model by considering the trigonal warping effect. Supplementary Figures 13(a) displays the HF ground state phase diagram with trigonal warping included. Compared to the Dirac fermion model without trigonal warping, the condensation energies of both types of WC ground states are significantly enhanced by the exchange effect. Additionally, the energy of the trivial WC consistently remains lower than that of the AHC ground state. Supplementary Figures 13(b) illustrates the ground

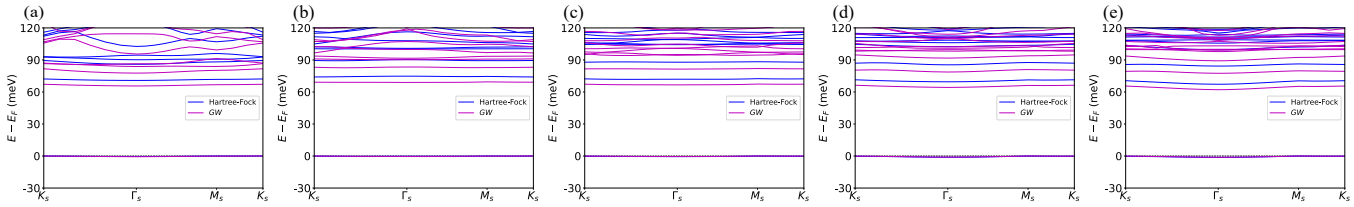

Supplementary Figure 12: (a)-(e) The GW-calculated single-particle energy spectra for the trivial WC state for n-order Dirac fermion models with $n = 2$ to 6 at $L_s = 200$ Å, respectively.

state phase diagram obtained from GW+RPA calculations. It is evident that when $L_s \lessapprox 750\,\mathring{A}$, the trivial WC remains the system's ground state. However, when $L_s \gtrapprox 750\,\mathring{A}$, the AHC state becomes energetically stabilized over the trivial WC, which is attributed to the lower correlation energy achieved by AHC through dynamical charge fluctuations.

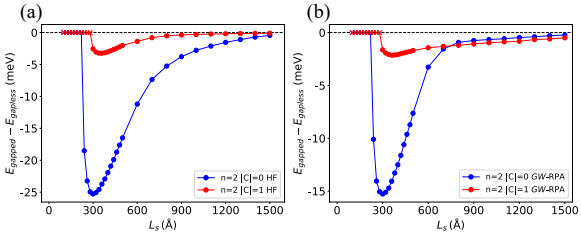

Supplementary Figure 13: (a)-(b) The HF and GW+RPA results for the WC condensation energy as a function of lattice constant L_s for bilayer graphene two band model, respectively.

D. Summary

In this section, we have presented a comprehensive analysis of n-order Dirac fermion models for $n = 2$ to 6 and the BLG two-band model with trigonal warping, exploring the ground state under both HF and the more advanced GW+RPA calculations. The HF results indicate that, with an increasing layer number, the WC state becomes more stable due to enhanced electron-electron interactions, with the trivial WC as the ground state in this context. However, the inclusion of RPA correlation energy in the GW+RPA framework reveals that correlation effects shift the WC phase transition point to a lower electron density and lower the total energy of the AHC below that of the trivial WC. This effect is particularly evident in the $n = 2$ system, where, at low electron densities, the correlation energy enables the AHC to surpass the trivial WC as the ground state. In the BLG two-band model with trigonal warping, the AHC is favored over the trivial WC at low density due to lower correlation energy gained from dynamical charge fluctuations. This finding underscores the indispensable role of correlation effects described by the GW+RPA approach in the study of the WC phase transition.

SUPPLEMENTARY REFERENCES

[S1] H. Min and A. H. MacDonald, Progress of Theoretical Physics Supplement **176**, 227 (2008).
[S2] J. Liu, Z. Ma, J. Gao, and X. Dai, Phys. Rev. X **9**, 031021 (2019).
[S3] X. Lu, S. Zhang, Y. Wang, X. Gao, K. Yang, Z. Guo, Y. Gao, Y. Ye, Z. Han, and J. Liu, Nature Communications **14**, 5550 (2023).
[S4] L. Hedin, Phys. Rev. **139**, A796 (1965).
[S5] M. S. Hybertsen and S. G. Louie, Phys. Rev. B **34**, 5390 (1986).
[S6] F. Aryasetiawan and O. Gunnarsson, Reports on Progress in Physics **61**, 237 (1998).
[S7] G. Onida, L. Reining, and A. Rubio, Rev. Mod. Phys. **74**, 601 (2002).
[S8] L. Reining, WIREs Computational Molecular Science **8**, e1344 (2018).
[S9] D. Golze, M. Dvorak, and P. Rinke, Frontiers in chemistry **7**, 377 (2019).
[S10] A. Bostwick, F. Speck, T. Seyller, K. Horn, M. Polini, R. Asgari, A. H. MacDonald, and E. Rotenberg, Science **328**, 999 (2010).

[S11] P. E. Trevisanutto, C. Giorgetti, L. Reining, M. Ladisa, and V. Olevano, Phys. Rev. Lett. **101**, 226405 (2008).
[S12] H. Zhang, S. Wang, E. Wang, X. Lu, Q. Li, C. Bao, K. Deng, H. Zhang, W. Yao, G. Chen, A. V. Fedorov, J. D. Denlinger, K. Watanabe, T. Taniguchi, G. Zhang, and S. Zhou, npj Quantum Materials **6**, 83 (2021).
[S13] D. A. Leon, C. Cardoso, T. Chiarotti, D. Varsano, E. Molinari, and A. Ferretti, Phys. Rev. B **104**, 115157 (2021).
[S14] D. A. Leon, A. Ferretti, D. Varsano, E. Molinari, and C. Cardoso, Phys. Rev. B **107**, 155130 (2023).
[S15] S. B. Zhang, D. Tománek, M. L. Cohen, S. G. Louie, and M. S. Hybertsen, Phys. Rev. B **40**, 3162 (1989).
[S16] R. W. Godby and R. J. Needs, Phys. Rev. Lett. **62**, 1169 (1989).
[S17] W. von der Linden and P. Horsch, Phys. Rev. B **37**, 8351 (1988).
[S18] G. E. Engel and B. Farid, Phys. Rev. B **47**, 15931 (1993).
[S19] R. Côté and A. H. MacDonald, Phys. Rev. B **44**, 8759 (1991).
[S20] A. L. Fetter and J. D. Walecka, Quantum theory of many-particle systems (Courier Corporation, 2012).
[S21] D. Bohm and D. Pines, Phys. Rev. **92**, 609 (1953).
[S22] M. Gell-Mann and K. A. Brueckner, Phys. Rev. **106**, 364 (1957).
[S23] X. Ren, P. Rinke, C. Joas, and M. Scheffler, Journal of Materials Science **47**, 7447 (2012).
[S24] N. D. Drummond and R. J. Needs, Phys. Rev. Lett. **102**, 126402 (2009).
[S25] F. Rapisarda and G. Senatore, Australian journal of physics **49**, 161 (1996).